Electronic Supplementary Material (ESI) for Energy & Environmental Science.

Supplementary Information

The operation active site of O_2 reduction to H_2O_2 over ZnO

Yunjie Zhou,[a] *Liang Xu,*[a] *Jie Wu,*[a] *Wenxiang Zhu,*[a] *Tiwei He,*[a] *Hao Yang,*[a] *Hui Huang,*[a] *Tao Cheng,**[a] *Yang Liu,**[a] and *Zhenhui Kang**[a, b]

[a] Institute of Functional Nano & Soft Materials (FUNSOM), Jiangsu Key Laboratory for Carbon-Based Functional Materials & Devices, Soochow University, Suzhou, 215123, Jiangsu, China.

[b] Macao Institute of Materials Science and Engineering (MIMSE), MUST−SUDA Joint Research Center for Advanced Functional Materials, Macau University of Science and Technology, Taipa 999078, Macao, China.

E-mail: tcheng@suda.edu.cn, yangl@suda.edu.cn, zhkang@suda.edu.cn

Supplementary Materials

Supplementary Text

Supplementary Figure 1 to 22

Supplementary Table 1 to 2

References

Materials and Methods:

$Zn(NO_3)_2 \cdot 6H_2O$ (99%) was purchased from Sigma-Aldrich; Urea (99.5 %) and K_2SO_4 (99%) were purchased from Sinopharm Chemical Reagent Co. Ltd (China); H_2O_2 (30%) was purchased from Yonghua Chemical Co., Ltd.; Nafion perfluorinated resin solution (5 wt %) was purchased from Adamas-Betas; Nafion 212 proton exchange membrane and Toray Carbon Paper (TGP-H-60) were purchased from Alfa Aesar. Milli-Q ultrapure water (Millipore, ≥18.2 MΩ cm^{-1}) was used throughout the work.

Pulse voltage-induced current (PVC)

According to S. Trasatti et al. [1,2], the voltammetrlc charge depends on the potential sweep, and the sweep−rate dependence of q^* is to be related to the existence of less accessible surface. Extrapolation of q* to ν = 0 provides q^*_T, the total charge proportional to the whole active surface. Conversely, extrapolation of q^* to $\nu = \infty$ provides q^*_O, which is related to the 'outer' active surface.

The relationship between q^* and scan rate ν has been found to be:

$$1/q^*(\upsilon) = q_T^* + k_1\upsilon^{1/2}$$

And the relationship between q^*O and scan rate has been found to be:

$$q^*(\upsilon) = q_O^* + k_2\upsilon^{-1/2}$$

The interfacial capacitance (C) can be been found to be:

$$C = \frac{\int_{E_2}^{E_1} |i| \mathrm{d}E}{2\upsilon(E_2 - E_1)} = \frac{\int_{E_1}^{E_2} |i_a| \mathrm{d}E + \int_{E_2}^{E_1} i_c \mathrm{d}E}{2\upsilon(E_2 - E_1)}$$

i_a and i_c are the instantaneous anodic and cathodic current, respectively, E_1 and E_2 are the cutoff potentials in the CVs.

The relationship between voltammetric charge and interfacial capacitance is:

$$q^*(v) = C(v) * (E_2 - E_1)$$

Similar to q^*_T and q^*_O, total capacitance C_T and outer capacitance C_O can be obtained by the following equations:

$$1/C(v) = 1/C_T + k_1' v^{1/2}$$

And:

$$C(v) = C_O + k_2' v^{-1/2}$$

DFT Calculations.

computational methods and models:

All calculations were carried out using the VASP (Vienna Ab-initial Simulation Package, VASP) software 5.4.4 [3–5], the exchange function was described by PBE (Perdew, Burke and Ernzerhof) functional parameterization of GGA (Generalized Gradient Approximation, GGA) [6] of DFT (Density of Functional Theory, DFT). What's more, these calculations took DFT-D3 correction for London disperse (van der Waals attraction) with Becke-Johnson damping into consideration [7]. And the PAW (Projector Augmented Wave) method was used to account for core-valence interactions [8,9]. The kinetic energy cutoff for plane wave expansions was set at 400 eV, and reciprocal space was sampled by the Γ-centered Monkhorst-Pack scheme with a grid of 3×3×1. The convergence criteria are 1 x 10^{-5} eV energy differences for solving the electronic wave function. All atomic coordinates were converged to within 1 x 10^{-2} eV $Å^{-1}$ for maximal components of force. Then, we carried out building models and simulations for three systems, including ZnO, ZnO_2, and ZnO@ZnO_2 to study the mechanism of ORR. ZnO slab was modeled by a 3 × 2 × 3 unit cell, ZnO_2 slab was modeled by a 2 × 2 × 3 unit cell, and the ZnO@ZnO_2 slab was derived from ZnO, which was added 6 O atoms placed on the surface among Zn atoms. And a vacuum thickness was set to 20 Å for these systems to remove any interactions between periodic slabs. First, optimize the intermediates during ORR. The atoms in the last layer were fixed on the three systems, and all the other atoms were relaxed. The applied voltage was corrected according to Computational Hydrogen Electrode (CHE) model proposed by Norskov et al [10,11]. In CHE, the Gibbs free energy of the proton-electron pairs ($H^+ + e^-$) is set to one-half of the Gibbs free energy of a hydrogen (H_2) molecule, ΔG(U) was corrected with am applied potential U can be defined as:

$$\Delta G(U) = \Delta G(0) - eU$$

Where the *-eU* term is the multiplication of electron charge and the applied potential (U).

Free energies were calculated as follows:

$$G_{298.15} = E_{elec} + E_{zpe} - T * S_m^v$$

The vibrational frequencies were evaluated for only surface adsorbate and calculated. According to

the results of the calculated frequency, we obtained the zero-point energy(zpe) that corrected the E_{elec} and absorption entropy S_m^v

$$S_m^V = \sum_{\tilde{\nu}}^{\tilde{\nu}t} R\{\frac{\beta hc\tilde{\nu}}{e^{\beta hc\tilde{\nu}}} - \ln(1 - e^{-\beta hc\tilde{\nu}})\}$$

Where R is gas constant, β is $1/T*K_b$ (K_b is Boltzman constant), h is Plank constant, c is light speed, and v is wave number.

All potential possibilities of oxygen molecules adsorbed on the ZnO@ZnO_2 interface are be explored, and Fig. S13 shows the simulation diagram of adsorption configurations of oxygen molecules at different sites. The results show that the oxygen adsorption configuration shown in Fig. S10 F has the lowest potential energy, i.e. the reaction site is the Zn atoms at the heterogeneous interface.

The formation energy of OOH* to O* on ZnO@ZnO_2 is higher than ZnO. Meanwhile, the formation energy of OOH* to *H_2O_2 (* denotes an unoccupied active site) on ZnO@ZnO_2 is smaller than that of ZnO and ZnO_2. The binding energy of HOO* (ΔG_{HOO*}) was an effective activity descriptor with an optimal value of ~4.2 eV. According to this guideline, the ΔG_{HOO*} of ZnO@ZnO_2 (ΔG_{HOO*} = 3.54 eV) is closer to the optimal value than ZnO (ΔG_{HOO*} = 2.37 eV) and ZnO_2 (ΔG_{HOO*} = 2.54 eV). Since the OOH* adsorption is present on both the $2e^-$ and $4e^-$ pathways, it is not the only factor affecting selectivity, as a weaker O* adsorption will effectively inhibit the conversion of OOH* to O* to obtain higher H_2O_2 selectivity. The dashed line in Fig. 2I represents the average value between the absorbed energy on Pt (classic $4e^-$ ORR catalyst; ΔG_{O*} = 1.58 eV) and on $PtHg_4$ (classic $2e^-$ ORR catalyst; ΔG_{O*} = 2.75 eV), which is a boundary (ΔG_{O*} = 2.165 eV) [12,13]. The binding energy of O* on ZnO@ZnO_2 (ΔG_{O*} = 2.92 eV), albeit not as positive as $PtHg_4$, has exceeded the boundary and was sufficiently large to render $2e^-$ ORR.

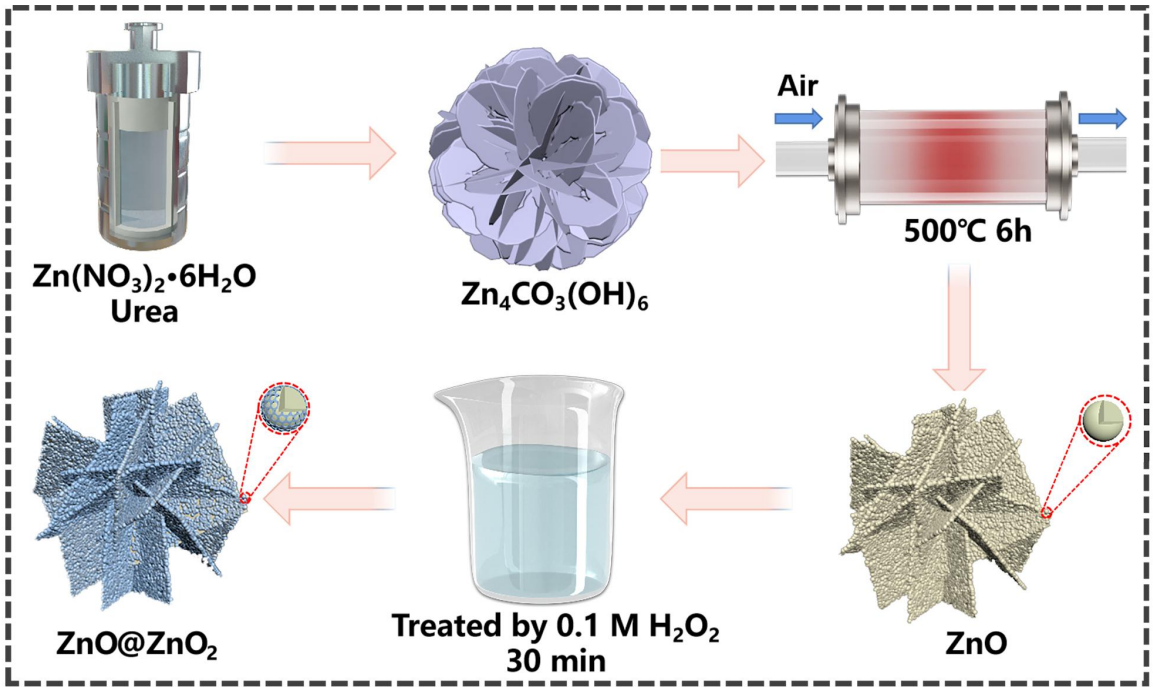

Fig. S1 Schematic illustration for the synthesis of $ZnO@ZnO_2$.

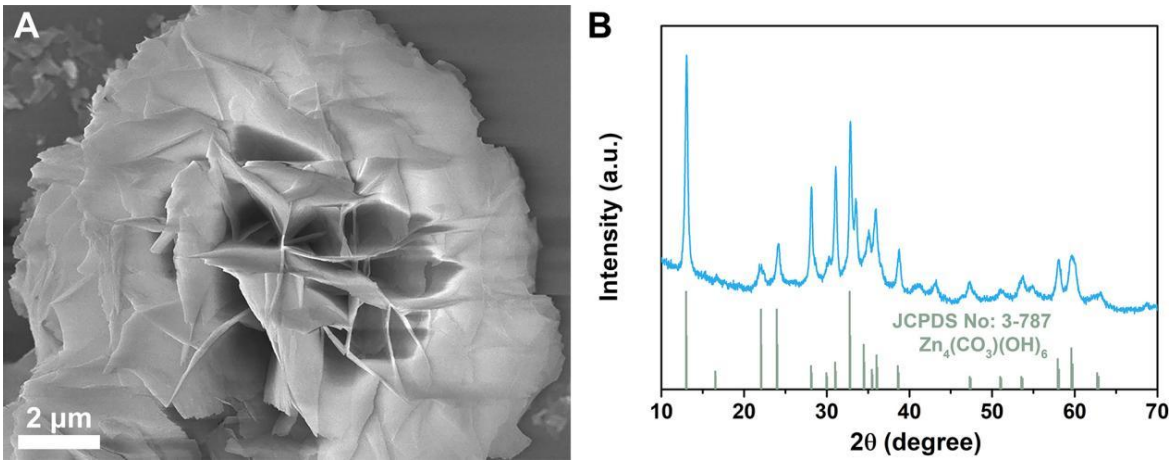

Fig. S2 (A) SEM image and (B) XRD pattern and standard card (JCPDS NO: 3-787) of $Zn_4CO_3(OH)_6$. The product obtained in the first step is flake nanostructure, which is shown to be $Zn_4CO_3(OH)_6$ by XRD.

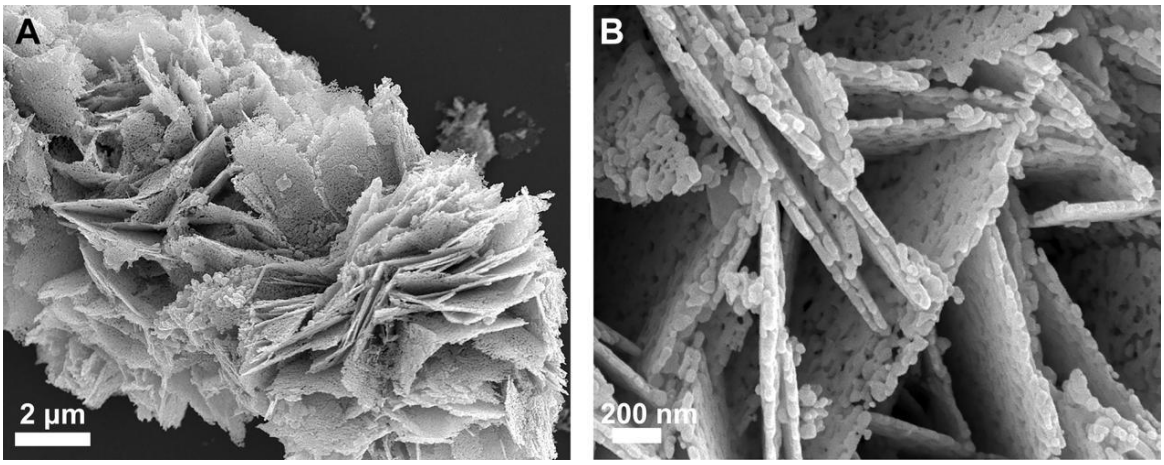

Fig. S3 SEM images of ZnO.

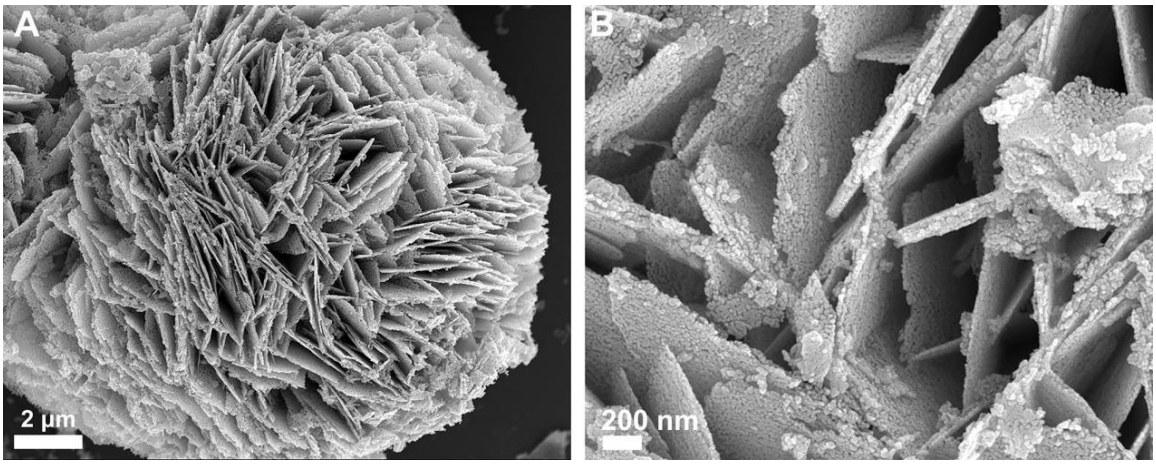

Fig. S4 SEM images of $ZnO@ZnO_2$.

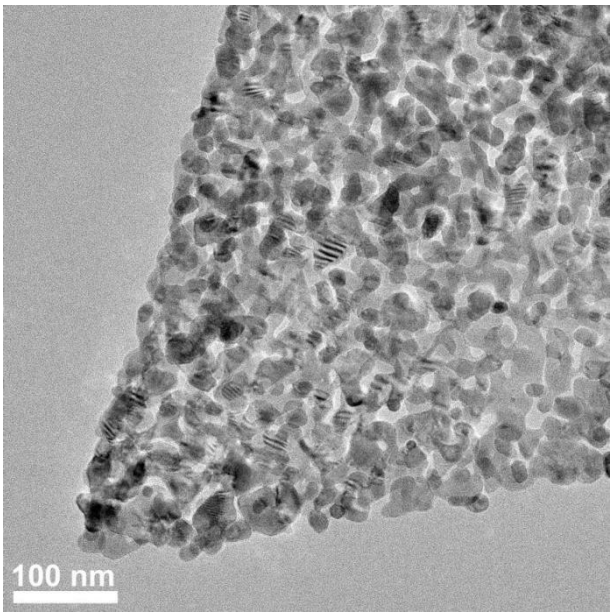

Fig. S5 TEM image of ZnO.

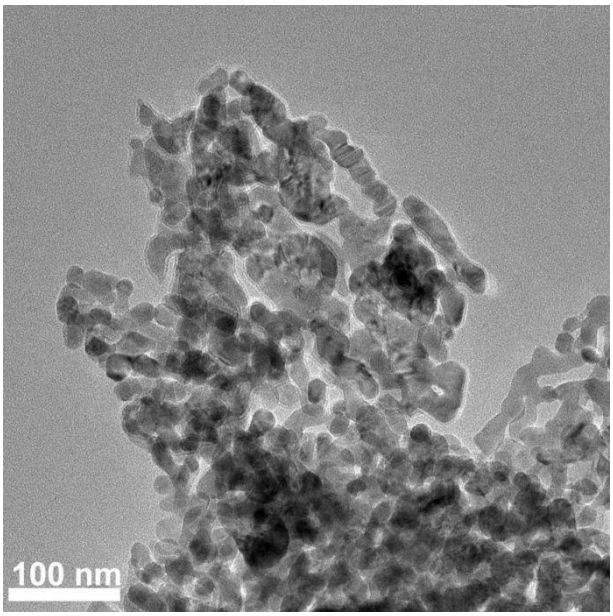

Fig. S6 TEM image of $ZnO@ZnO_2$.

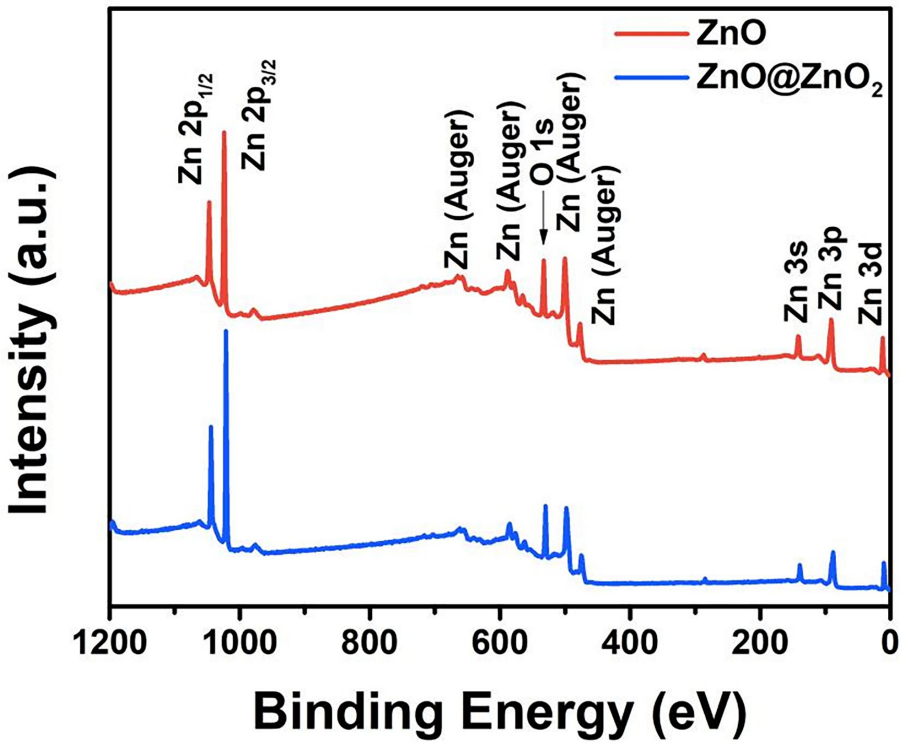

Fig. S7 XPS survey spectra of ZnO and ZnO@ZnO_2.

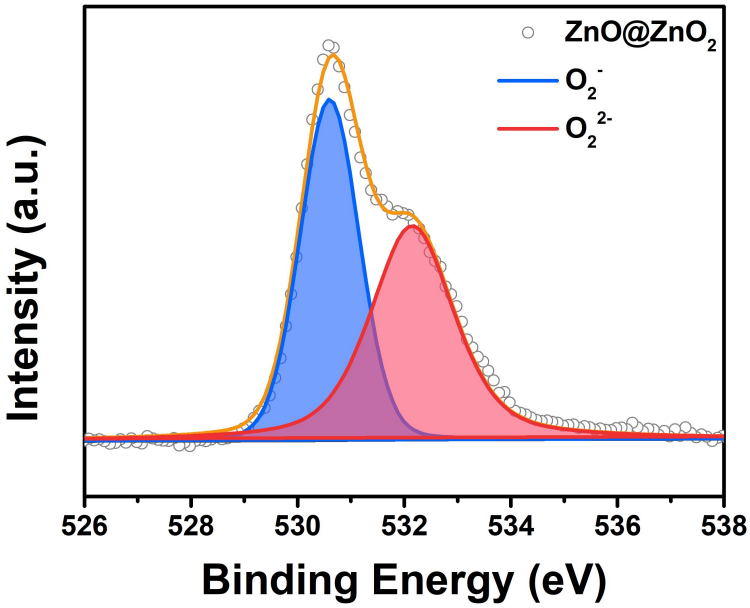

Fig. S8 Fitted peaks of O 1s spectrum of $ZnO@ZnO_2$.

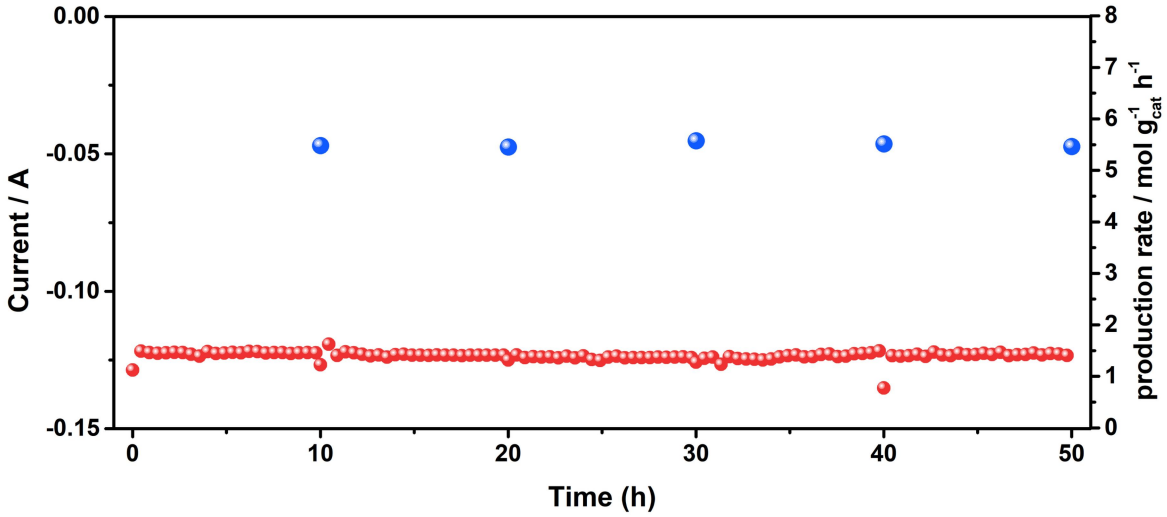

Fig. S9 I - t curves and H_2O_2 production rate of ZnO@ZnO_2 @ 0.1 V vs. RHE. The electrolyte solution is renewed every 10 hours.

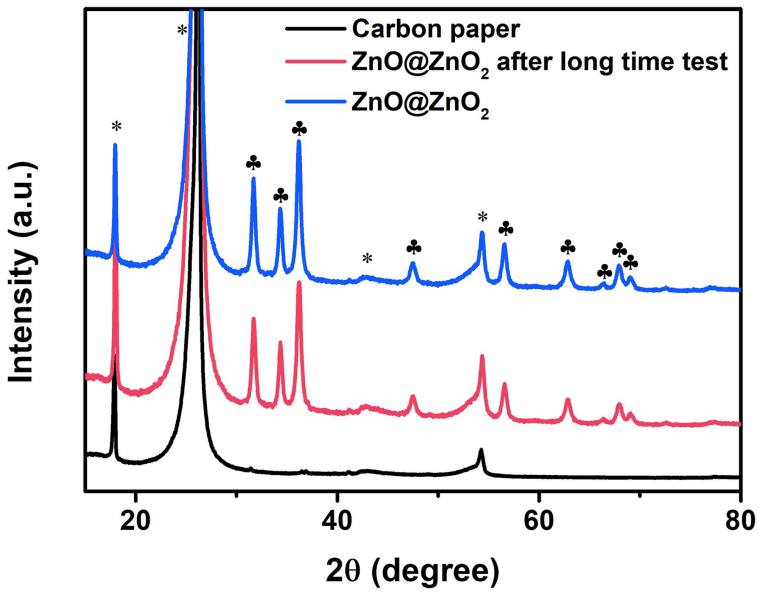

Fig. S10 XRD patterns of carbon paper, $ZnO@ZnO_2$ loaded on carbon paper before and after long time test.

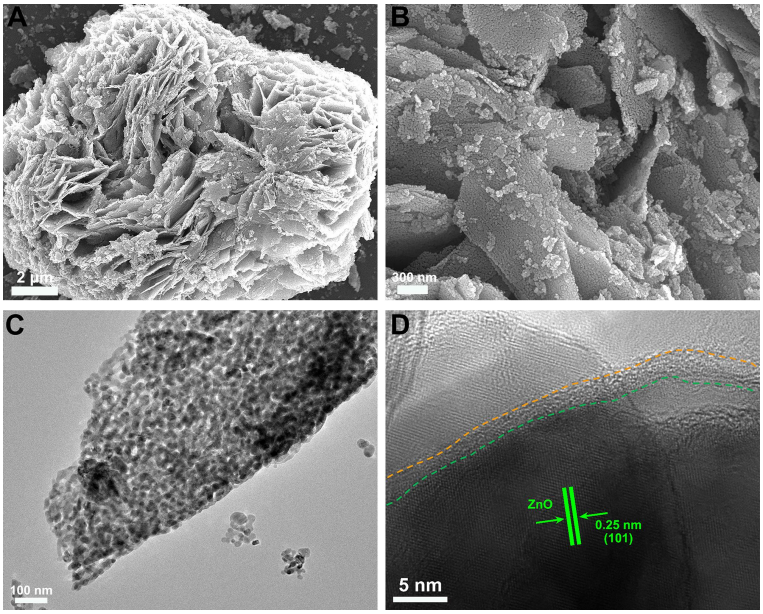

Fig. S11 (A, B) SEM image of $ZnO@ZnO_2$ after long-term cycles. (C, D) TEM and HRTEM images of $ZnO@ZnO_2$ after long-term cycles.

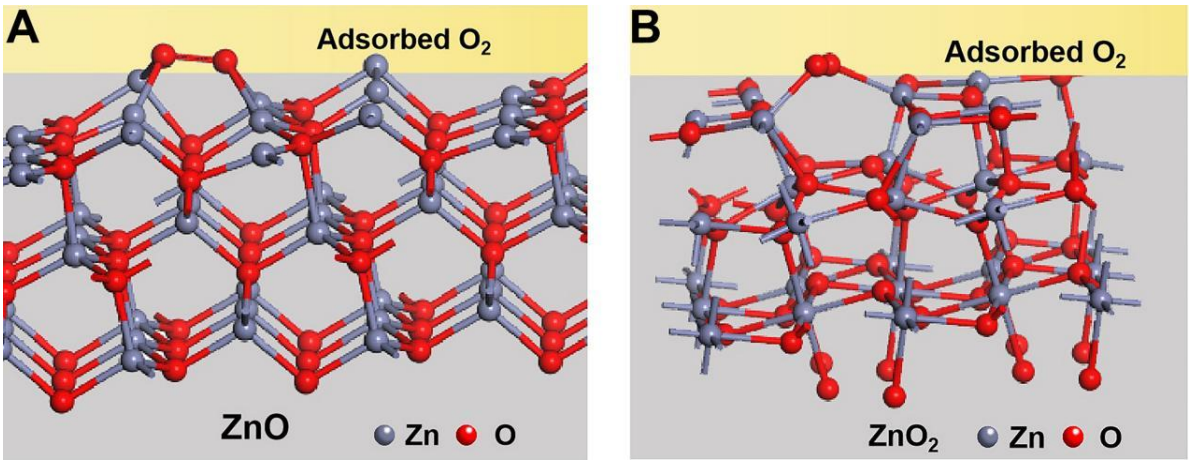

Fig. S12 Adsorption model of O_2 molecule on ZnO and ZnO_2; red and gray spheres represent O and Zn atoms, respectively.

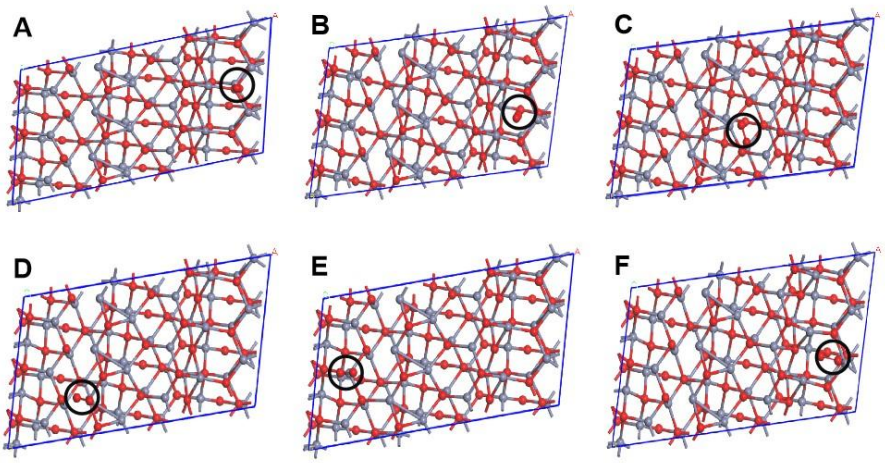

Fig. S13 TOP view of adsorption configuration of oxygen molecules at different sites of ZnO@ZnO_2. (A) Top site on O (-511.237 eV), (B) Hollow site (-511.280 eV), (C) Bridge site I (-511.287 eV), (D) Bridge site II (-511.241 eV), (E) Top site on Zn I (-511.458 eV), (F) Top site on Zn II (-511.581 eV).

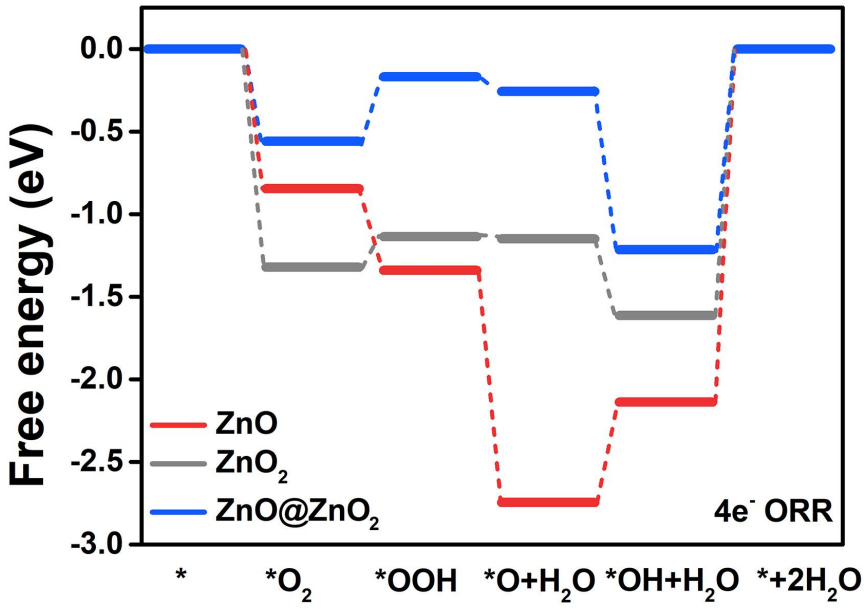

Fig. S14 $4e^-$ ORR pathway on ZnO, ZnO_2 and ZnO@ZnO_2 (*U*: 0.7 V).

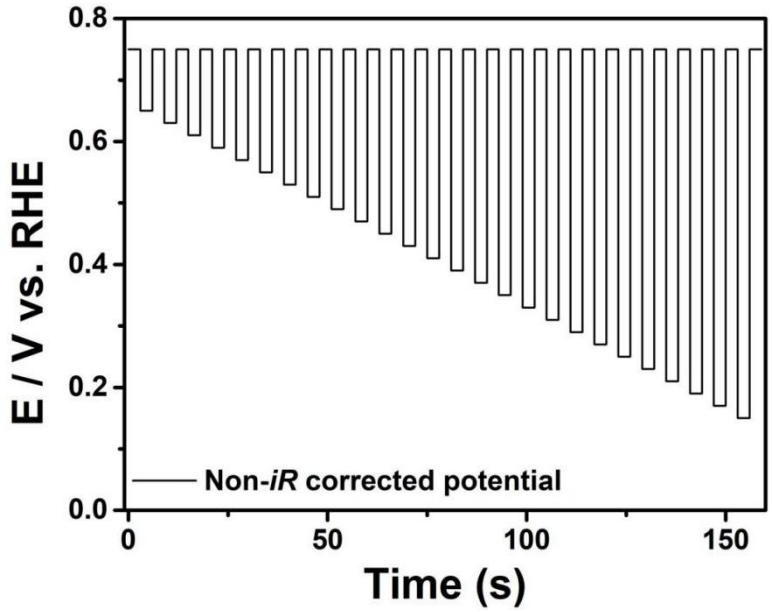

Fig. S15 Pulse voltammetry protocol between 0.75 V vs. RHE anodic and 0.65 V to 0.15 V vs. RHE cathodic non−iR corrected potentials.

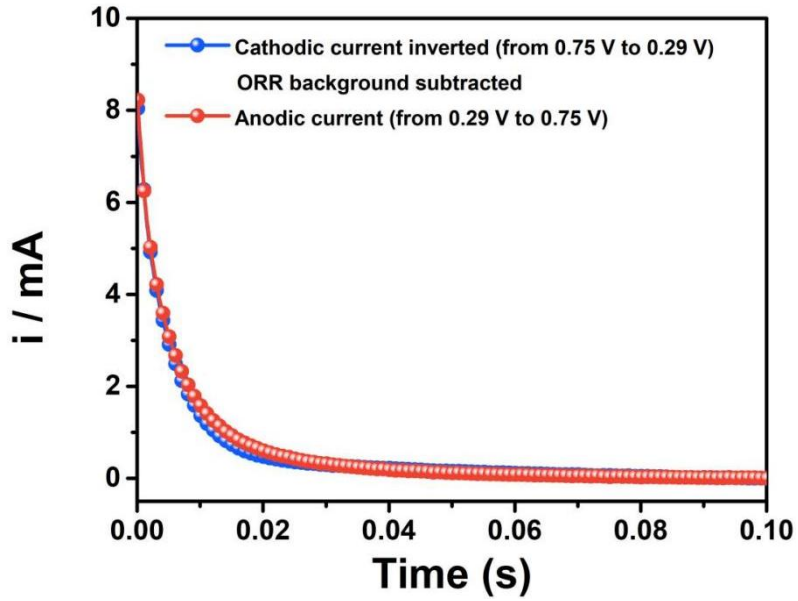

Fig. S16 Inverted cathodic current decay after background subtraction (step from 0.75 V to 0.29 V) and the anodic current signal upon the reverse (0.29 V to 0.75 V) of ZnO@ZnO_2.

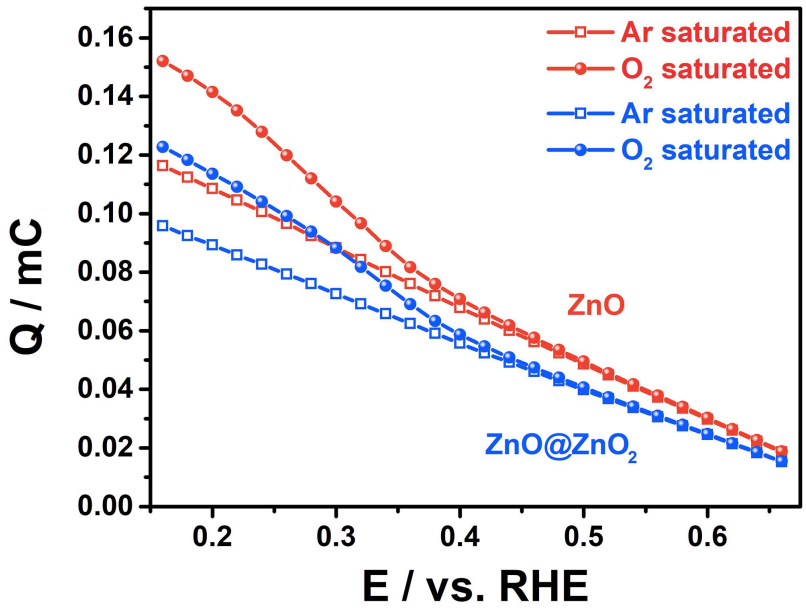

Fig. S17 Charge versus potential from PVC of ZnO and ZnO@ZnO_2 in O_2 and Ar saturated 0.1 M K_2SO_4.

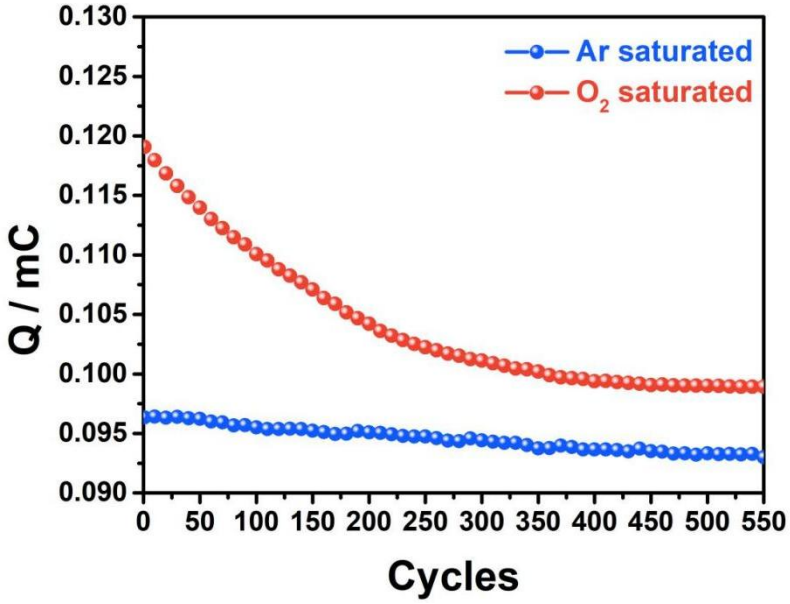

Fig. S18 Charge of ZnO during 550 cyclic PVC in O_2 or Ar saturated 0.1 M K_2SO_4. It is calculated at intervals of 10 cycles to obtain the value of charge stored by ZnO.

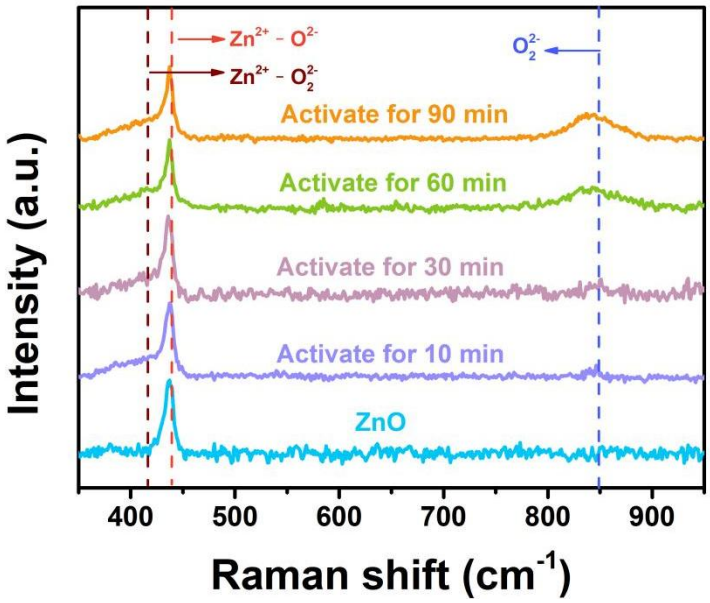

Fig. S19 Raman spectra of ZnO electrically activated for different times.

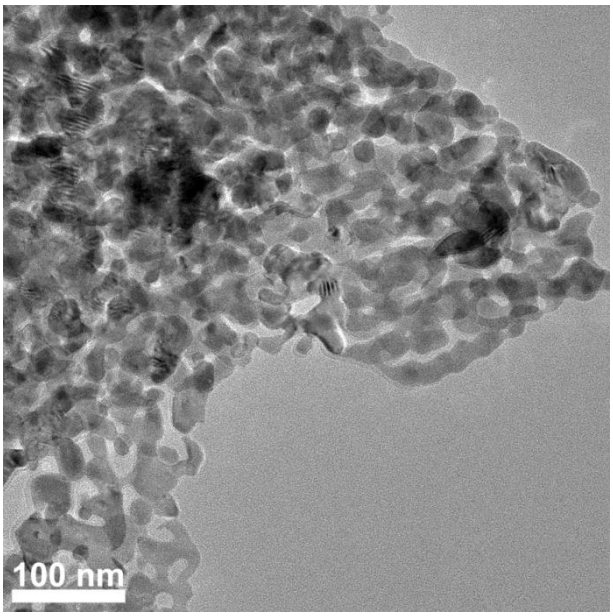

Fig. S20 TEM image of ZnO treated by 10 mmol•L^{-1} H_2O_2.

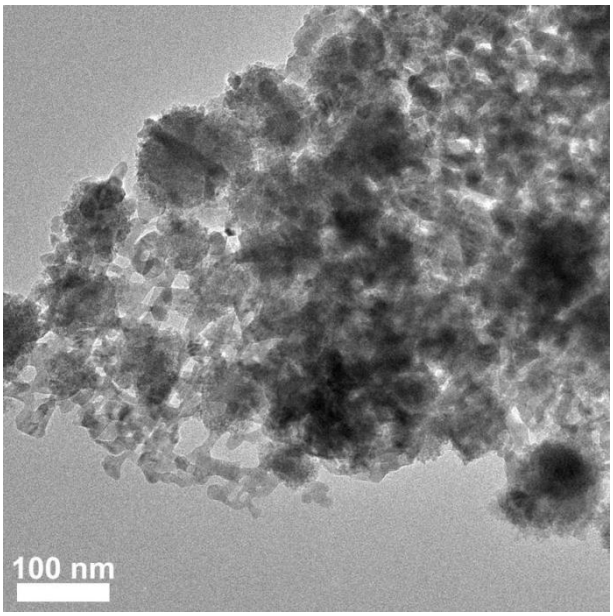

Fig. S21 TEM image of ZnO treated by 0.4 mol•L^{-1} H_2O_2.

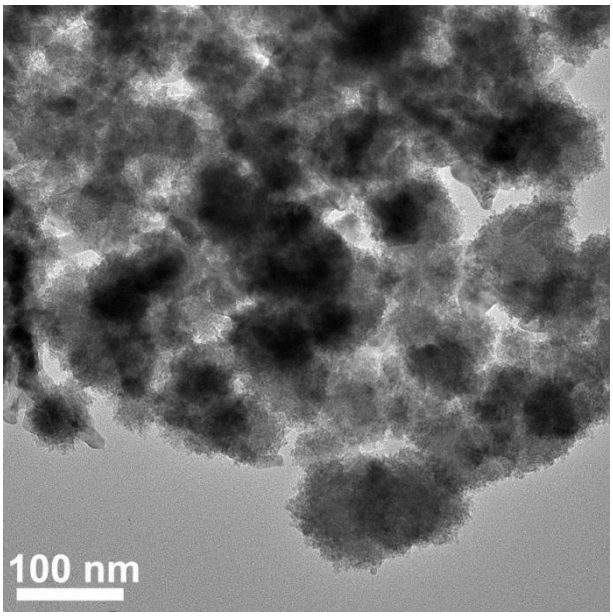

Fig. S22 TEM image of ZnO treated by 1.6 mol•L^{-1} H_2O_2.

Table S1. The comparison of $2e^-$ ORR performance in neutral solution.

Material	Electrolyte	Selectivity	1 mA cm^{-2}	Oneset potential	Ref.
ZnO@ZnO_2	**0.1 M K_2SO_4**	**~100%**	**0.38**	**0.5**	**This work**
Co/NC	0.1 M PBS	>90%	0.72	0.8	[14]
O-BC-3h	0.1 M PBS	75-80%	0.357	0.47	[15]
HPC-H24	0.1 M Na_2SO_4	70.2-85.1%	0.47	0.55	[16]
PCMNS	0.1 M K_2SO_4	86.7-93.3%	0.41	0.49	[17]
Pd-Se-B NC	0.1M KPI	80-90%	0.55	0.7	[18]
PR-25/Silica-700	0.1 M K_2SO_4	80-90%	0.41	0.5	[19]
MHCS-9:1	0.1M PBS	>90%	0.51	0.62	[20]
N-CNT	0.1M PBS	90-94.2%	0.38	0.75	[21]
CoS_2	0.05 M Na_2SO_4	<50%	0.5	0.54	[22]
Fe-CNT	0.1 M PBS	80-100%	0.41	0.53	[23]
GOx/$MnCO_3$	3.5% NaCl	~50%	0.4	0.635	[24]
O-CNT	0.1M PBS	85%	0.32	0.5	[25]
PEI50CMK3_800T	0.1 M K_2SO_4	89.8%	0.32	0.52	[26]

Table S2. The comparison of H_2O_2 production rates of ZnO@ZnO_2 with recently reported ORR catalysts in neutral solution.

Material	Electrolyte	Condition	Productivity (mol g^{-1}_{cat} h^{-1})	Faradaic efficiency (%)	Ref.
ZnO@ZnO_2	**0.1 M K_2SO_4**	**0.1V**	**5.47**	**95.5%**	**This work**
Co/NC	0.1 M PBS	0.3V	3.57	84.2%	[14]
O-BC-3h	0.1 M Na_2SO_4	50 mA cm^{-2}	1.525	65.4%	[15]
HPC-H24	0.1 M Na_2SO_4	0.15V	0.1102	70.8%	[16]
PCMNS	0.1 M K_2SO_4	0.35V	1.1025	-	[17]
PR-25/Silica-700	0.1 M PBS	0V	1.27	>90%	[19]
N-CNT	0.1 M PBS	0.15V	4.45 mmol $h^{-1}L^{-1}$	89.5%	[21]
PEI50CMK3_800T	0.1 M K_2SO_4	0.2V	0.571	37-65%	[26]
N-CBMC-500	0.5 M Na_2SO_4	-0.65V	2.46	70%	[27]

Reference:

1 C. P. De Pauli and S. Trasatti, *J. Electroanal. Chem.*, 1995, **396**, 161–168.

2 S. Ardizzone, G. Fregonara and S. Trasatti, *Electrochimica Acta*, 1990, **35**, 263–267.

3 G. Kresse and J. Hafner, *Phys. Rev. B*, 1993, **47**, 558–561.

4 G. Kresse and J. Furthmüller, *Comput. Mater. Sci.*, 1996, **6**, 15–50.

5 G. Kresse and J. Furthmüller, *Phys. Rev. B*, 1996, **54**, 11169–11186.

6 J. P. Perdew, K. Burke and M. Ernzerhof, *Phys. Rev. Lett.*, 1996, **77**, 3865–3868.

7 S. Grimme, J. Antony, S. Ehrlich and H. Krieg, *J. Chem. Phys.*, 2010, **132**, 154104.

8 P. E. Blöchl, *Phys. Rev. B*, 1994, **50**, 17953–17979.

9 G. Kresse and D. Joubert, *Phys. Rev. B*, 1999, **59**, 1758–1775.

10 J. Durst, A. Siebel, C. Simon, F. Hasché, J. Herranz and H. A. Gasteiger, *Energy Env. Sci*, 2014, **7**, 2255–2260.

11 G. T. K. K. Gunasooriya and J. K. Nørskov, *ACS Energy Lett.*, 2020, **5**, 3778–3787.

12 S. Siahrostami, A. Verdaguer-Casadevall, M. Karamad, D. Deiana, P. Malacrida, B. Wickman, M. Escudero-Escribano, E. A. Paoli, R. Frydendal, T. W. Hansen, I. Chorkendorff, I. E. L. Stephens and J. Rossmeisl, *Nat. Mater.*, 2013, **12**, 1137–1143.

13 X. Zhao, Y. Wang, Y. Da, X. Wang, T. Wang, M. Xu, X. He, W. Zhou, Y. Li, J. N. Coleman and Y. Li, *Natl. Sci. Rev.*, 2020, **7**, 1360–1366.

14 H. Shen, N. Qiu, L. Yang, X. Guo, K. Zhang, T. Thomas, S. Du, Q. Zheng, J. P. Attfield, Y. Zhu and M. Yang, *Small*, 2022, **18**, 2200730.

15 S. Wang, D. Ye, H. Liu, X. Zhu, Z. Liu, R. Chen, Q. Liao and Y. Yang, *Int. J. Hydrog. Energy*, 2022, **47**, 5961–5973.

16 Y. Liu, X. Quan, X. Fan, H. Wang and S. Chen, *Angew. Chem. Int. Ed.*, 2015, **54**, 6837–6841.

17 R. Hu, Y. Cui, B. Huang and L. Guan, *ACS Appl. Mater. Interfaces*, 2021, **13**, 35856–35864.

18 J. Lee, S. W. Choi, S. Back, H. Jang and Y. J. Sa, *Appl. Catal. B Environ.*, 2022, **309**, 121265.

19 B. Huang, Y. Cui, R. Hu, J. Huang and L. Guan, *ACS Appl. Energy Mater.*, 2021, **4**,

4620–4629.

20 Y. Pang, K. Wang, H. Xie, Y. Sun, M.-M. Titirici and G.-L. Chai, *ACS Catal.*, 2020, **10**, 7434–7442.

21 S. Ren, W. Cui, L. Li and Z. Yi, *Sustain. Energy Fuels*, 2021, **5**, 6310–6314.

22 H. Sheng, E. D. Hermes, X. Yang, D. Ying, A. N. Janes, W. Li, J. R. Schmidt and S. Jin, *ACS Catal.*, 2019, **9**, 8433–8442.

23 K. Jiang, S. Back, A. J. Akey, C. Xia, Y. Hu, W. Liang, D. Schaak, E. Stavitski, J. K. Nørskov, S. Siahrostami and H. Wang, *Nat. Commun.*, 2019, **10**, 3997.

24 N. Wang, S. Ma, J. Duan, X. Zhai, F. Guan, X. Wang and B. Hou, *Electrochimica Acta*, 2020, **340**, 135880.

25 Z. Lu, G. Chen, S. Siahrostami, Z. Chen, K. Liu, J. Xie, L. Liao, T. Wu, D. Lin, Y. Liu, T. F. Jaramillo, J. K. Nørskov and Y. Cui, *Nat. Catal.*, 2018, **1**, 156–162.

26 Y. Sun, S. Li, Z. P. Jovanov, D. Bernsmeier, H. Wang, B. Paul, X. Wang, S. Kühl and P. Strasser, *ChemSusChem*, 2018, **11**, 3388–3395.

27 Z. Bao, J. Zhao, S. Zhang, L. Ding, X. Peng, G. Wang, Z. Zhao, X. Zhong, Z. Yao and J. Wang, *J. Mater. Chem. A*, 2022, **10**, 4749–4757.